Synchrotron CT Imaging of Lattice Structures with Engineered Defects

Brian M. Patterson[1,2*], Lindsey Kuettner[1], Trevor Shear[1], Kevin Henderson[1], Matthew J. Herman[1], Axinte Ionita[3], Nikhilesh Chawla[4], Jason Williams[4], Tao Sun[5,^], Kamel Fezzaa[5], Xianghui Xiao[5,#], Cynthia Welch[1]

[1]Engineered Materials Group, Materials Science and Technology Division, Los Alamos National Laboratory, Los Alamos, NM 87545

[2] Institute for Materials Science, Los Alamos, NM 87545

[3] Physics and Chemistry of Materials Group, Theoretical Division, Los Alamos National Laboratory, Los Alamos, NM 87545

[4] Center for 4D Materials Science, Arizona State University, Tempe, Arizona 85281

[5] Advanced Photon Source, Argonne National Laboratory, Argonne, IL 60439

[^] Current affiliation: School of Engineering and Applied Science, University of Virginia, Charlottesville, VA 22904

[#] Current affiliation: National Synchrotron Light Source II, Brookhaven National Laboratory, Upton, NY, 11973, USA

Abstract

Understanding mechanical failure, crack propagation, and compressive behavior at the micrometer scale is essential for tailoring material properties for structural performance in cellular materials. Typically, modeling of traditional polymer foam materials is clouded by the lack of control in material morphology and its inherent stochastic structure. Additive manufacturing with sub-micrometer resolution provides a direct path for experimenters to specifically tailor structures needed by modelers to explicitly probe mechanical performance. Using laboratory-based 3D X-ray computed tomographic imaging (CT), the examination of deformation and damage provides a critical path to understanding how these soft materials behave. Additionally, synchrotron CT yields realistic information at higher strain rates to directly validate the robustness of our finite element modeling. For this study, nanolithographic printing was employed to generate a series of engineered lattices with increasing levels of defects through the random removal of ligaments. These structures were mechanically tested and imaged with laboratory-based microCT. Additionally, synchrotron experiments were conducted in which the structures were imaged in 3D at 14 Hz during compression at a 0.4 s^{-1} strain rate. These 3D images show the changes in the structure as the ligaments bend, buckle and fracture in real-time. This technique provides a robust framework for developing our methodologies and future exploration of engineered structures.

***Corresponding author:** bpatterson@lanl.gov, (505) 500-2726;

Keywords: X-ray tomography, microlattice, nanolithographic printing, finite element modeling

Introduction:

The elucidation of how the 3D structure of a porous material affects its mechanical properties [1] and how that relationship changes with age and/or use cycles is often complicated by the stochastic nature of a typically foamed material's structure. Historically, uncovering the structure-property relationships within such materials is difficult in that the morphology is only moderately controllable. With chemistry, a density of polymeric foams may be targeted, but the packing of the voids in porous materials is often completely random, resulting in material ligaments with variable length, orientation, connectivity, and cross-sectional shape. Even in materials with a roughly uniform density, the pore size distribution can be quite disperse [2-5]. Because equations derived to explain the mechanical relationships in cellular materials are based upon idealized structures [6], designing materials to meet compressive strength requirements is hampered.

With recent advances in additive manufacturing, we can now create specific, idealized foam structures that can be used to directly test and relate mechanical deformation to changes in the material structure. Ligament length, thickness, orientation, cross sectional shape, and connectivity can be designed and 3D-printed, thereby enabling control at the individual ligament level. Using a variety of 3D printing technologies, the material composition and size scale can also be controlled with robust repeatability and systematic variations. This level of control provides a means to scientifically probe the geometry of materials that gives rise to the mechanical properties and failure mechanisms. Cellular materials can not only be made of specific, designed structures, but these structures can be varied for degrees of lattice completeness. For example, we can remove a feature from a designed structure, such as a single lattice ligament or an entire class of lattice ligaments, and probe its role in determining the overall mechanical properties.

Polymer additively manufactured foam structures can be made with most of the 3D printing techniques [7,8]. Unfortunately, many polymer 3D printers use a layer-by-layer technique that suffers from an incomplete bonding between the layers. That is, there is little polymer-chain entanglement between the layers, leading to a structure that is weaker than those made through traditional manufacturing techniques. Techniques are being developed that do not suffer from this problem including the Continuous Liquid Interface Production (CLIP) process [9], a mobile liquid interface method [10], and the 2-photon polymerization (2PP) process [11]. 2PP uses a femtosecond laser and an optic to focus the laser energy into a sub-diffraction-limited spot to polymerize the resin. With this technique, volume pixel (voxel) sizes down to 100 nm are possible, yielding a much higher resolution than most other 3D printing techniques. A combination of laser- and sample-rastering is then used to write a 3D structure within the monomer resin, which is typically acrylate-based. Creating a lattice geometry with highly uniform morphological features is relatively straightforward [12] in both 3D printed polymers and metals. These small, simple structures can be used to examine local deformations to better understand the robustness of a finite element model. However due to limitations in either print time or 3D imaging volume, scientists are often left with small samples that suffer from issues at the boundaries and may experiments may not completely represent the mechanical performance of a much larger structure. These boundary conditions [13,14] exist at both the sample/platen interface [15] and lattice structure edges. Often constraints are applied at the sample interfaces [16,17] within the FEM.

During loading, the stiffness in polymers [18,19], metals [20-22], and especially polymeric cellular materials [23] increases with increased strain rate. The deformation in

polymers may proceed very differently than it does in metals. Depending upon this strain rate, the material may no longer behave in a linear-elastic fashion, but in a more complicated viscoelastic regime. To capture this viscoelastic deformation, a variety of techniques are used, including in situ photographic imaging and X-ray tomography. These are coupled with advanced image analysis techniques, including digital image correlation [24,25] and its 3D analogue, digital volume correlation [26,27]. These techniques can be used to better understand the effects of the printing parameters on material properties and subsequently increase mechanical properties such as fracture toughness [28]. By combining the structural control afforded by 3D printing and the enhanced understanding of structure-property relationships provided by in situ characterization methods, lattice materials can be fabricated with optimized mechanical properties that could never be achieved using traditional manufacturing techniques.

In the study reported herein, we take advantage of two major strengths of the 2PP technique in order to systematically study damage in cellular materials through the use of X-ray CT and finite-element modeling (FEM). First, the lattices can be printed multiple times for repeat experiments with a level of similitude that is often not achievable using a traditionally manufactured material. Second, the 2PP technique can create structures at such a high resolution that the entire structure can be imaged within the synchrotron beam at the Advanced Photon Source (maximum field-of-view is ~1 cm wide, ~4 mm tall). No information on the deformation of the structure is lost outside of the field-of-view; there are very few printing techniques that meet these requirements. Thus, a series of 3D-printed lattices, constructed of cubic unit cells including the face and body diagonals connecting each corner, was created with an increasing percentage of randomly removed ligaments. In this way, we explored the effects of defects, defined as ligaments removed from the ideal structure, on the mechanical properties of the structure. Using laboratory-based micro CT, we collected 3D images before and after loading to 15 % compression. Additionally, we collected stress-strain data on the various lattice structures. To understand the deformation of the material in situ, the material was compressed during synchrotron-based, rapid X-ray CT imaging. These lattice structures were computationally examined using finite element modeling (FEM). FEM meshes were created from the X-ray CT data and then the compression performance and deformation modeled. These experiments outline a framework to explore more creative and unique foam lattice geometries in order to better understand how to tune the fundamental design parameters to produce foams with explicitly optimized properties.

Experimental:

Sample Design

Using Autodesk Inventor Professional 2016 (Autodesk, Inc.) CAD software, we designed lattice structures in which the ligaments could be individually removed. Each sample contained eight cubic unit cells, which included the face and body diagonals connecting each corner, to construct the lattice structure with total sample dimensions of 600 μm x 600 μm x 600 μm. The structure is made up of 54 x-, y-, or z-oriented ligaments (red "vertical" and green "horizontal" in Figure 1 and Table 1), 72 45^{o}-oriented ligaments (yellow "cross"), and 32 central ligaments (orange), for a total of 158 ligaments within the complete structure. Five different lattice designs were created by randomly removing ligaments in an independent fashion, i.e., each design was randomly generated from the "defect-free" lattice. Table 1 outlines the randomly missing ligaments and Figure 1 graphically shows the ligament classes. Due to the low number of ligaments within the structure, the true percent missing was 0, 5.1, 10.1, 14.6, and 25.3%. The

designs were saved as STL files and imported into Nanoscribe's proprietary control software 'DeScribe'. Due to the size of the lattice design, stitching was required in order to manufacture the lattice structures.

Table 1: Breakdown of the classes of missing ligaments. See Figure 1 for the color guide to which ligaments are missing. For no 'class' was more than 50% of the ligaments removed.

Percent Missing	Vertical Top	Vertical Bottom	Horizontal Top	Horizontal Middle	Horizontal Bottom	Top cross	Middle cross	Bottom cross	Top cross outer	Bottom cross outer	Top inner cross	Bottom inner cross	Central Top	Central Bottom	Total Missing
0%	9	9	12	12	12	8	8	8	16	16	8	8	16	16	0
5.1%	8	9	12	12	12	6	7	8	16	14	6	8	16	16	8
10.1%	8	9	10	11	10	8	8	7	15	15	6	6	14	15	16
14.6%	7	8	9	11	8	8	8	7	14	12	8	8	14	13	23
25.3%	8	7	6	9	8	6	5	7	13	11	6	7	12	13	40
Total # of ligaments for each class	9	9	12	12	12	8	8	8	16	16	8	8	16	16	

Two Photon Lithography Printing

All lattice structures used in this work were produced using a Nanoscribe Photonics Professional GT from Nanoscribe GmbH (Eggenstein-Leopoldshafen, Germany). This instrumentation utilizes a Toptica, Erbium-doped-fiber laser at 780 nm ± 10 nm with a pulse length of < 120 fs, repletion rate of 80MHz ± 1MHz, operated at a power of 60 mW. 2PP relies on the simultaneous absorption of two individual photons to generate a radical at the extreme focal point of the laser. This mechanism allows for a resolution with voxel sizes as low as 100 nm, which is below the diffraction limit of the optical objective used to focus the laser. This voxel is then rastered through the polymer resin using a galvo-mirror system, building a 3D part by selectively polymerizing material within the print volume. This commercial system allows for the direct input of designs generated in CAD (computer aided design) software. The printing methodology used in this work takes advantage of the Photonics Professional GT in Dip-in Laser Lithography (DiLL) mode. An oil immersion objective, numerical aperture 0.8, was immersed directly into IP-S, Nanoscribe's commercially available monomer resin system, and lattices were manufactured by laser exposure at 40% of the available 60mW laser power and a scan speed of 10,000 µm/sec. With these conditions, the print voxel size was ~300 nm, therefore the vertical struts are ~100 print voxels wide. The sloped struts are a little wider. These structures required 13-18 hours to print, depending upon the number of missing ligaments. After the printing was completed, excess monomer resin was removed from the sample by submerging in propylene glycol methyl ether acetate (PGMEA) for 30 minutes followed by 2-propanol for an additional 30 minutes. Single prints were completed for the mechanical testing studies of the 5.1 and 25.3% lattices; two prints were completed of each of the 0, 10.1, and 14.6% lattices. These were each

tested mechanically. Additional prints were completed for further testing of the 0% and the 25.3% for the synchrotron studies and high resolution imaging. The printer prints the structure inverted, that is the substrate is upside down with the IP-S hanging below. The substrate and printed prints were then flipped over for CT imaging. Therefore, the labeling convention used here is that the 'top' in the CT images, during compression, and modeling was really the bottom, furthest away from the substrate, and was the last to print.

Lab-based Tomographic Imaging

The lab-based X-ray CT images were collected using a Carl Zeiss X-ray Microscopy Inc. (Pleasanton, CA) Xradia microXCT. Operating conditions include a W anode X-ray source in a cone beam geometry with an applied voltage of 40 kVp and applied current of 245 μA, 10 W power, camera binning of 2, 20X objective lens, and a 15 s exposure per radiograph. The sample was rotated 182° per tomogram to collect 2001 radiographs with a pixel size of 1.107 μm at the sample. Each image took nearly 8.5 hours to collect. Tomographic reconstruction was performed using Xradia XMReconstructor software. One replicate of each sample design was placed within a 500-N Deben load cell (model CT500 500N), which was then placed within the microCT for pre- and post- compression 3D imaging (Figures 2 and 3). The load cell was modified with ABS plastic platens (10 mm cross-sectional diameter) in order to improve the 3D images at the sample-platen interface; plastic platens have less X-ray absorption than the standard metal platens and less X-ray attenuation near the interface due to the cone-beam geometry of the instrument. The targeted compression was ~15% strain, which was chosen to clearly identify which ligaments were distorted by the compression. Additionally, a high resolution image was collected using the 20X with a binning of 1, with a voxel size of 0.59 μm to more precisely measure the uniformity of the strut diameter.

Compressive Stress-Strain Measurements

Because of the small sample size and low force (1-3 N) required to compress the samples, the Deben load cell was not used for the stress-strain measurements. Instead, a nano-mechanical test stage (Zeiss X-ray Microscopy Inc., Pleasanton, CA) with a maximum compressive force of 9 N [1] was used. However, prior to mechanical testing, every sample was imaged to a) assure print quality and b) ensure that each sample received an equal dose of X-rays, which may affect the degree of polymerization and, therefore, the mechanical properties. After imaging, samples were placed on the lower anvil of the nano-mechanical load cell and then brought into contact with the top anvil with a 10 mN pre-load force. For compressive modulus measurements, the samples were cyclically loaded to 5% strain five times at a strain rate of 0.005 s^{-1}. The same test specimen was then cyclically loaded to 15% strain five times, followed by a 50% strain one time. An example of this complete loading profile is shown in Figure 4 for the 10.1% missing sample. In order to calculate the engineering stress and engineering strain of each lattice specimen, a solid cross-section of 600 x 600 μm was assumed for each sample. The Young's modulus E was then calculated for each sample using the linear region of the stress vs. strain curve; values from each 5% strain loading and the first 15% loading were averaged together to calculate an average E for each lattice specimen. Additionally, a small camera was used to image the foam during loading.

Dynamic Mechanical Analysis

To obtain mechanical property parameters needed for the FEM modeling, bulk thin film samples were produced by depositing ~25 ml of the IP-S resin onto a glass slide and exposing to UV light at 365 nm for 30 minutes to polymerize the resin. Five such bulk samples were tested with a Q800 Dynamic Mechanical Analyzer (TA Instruments, New Castle, DE) with the film tension clamp. Strain sweeps were conducted at a frequency of 1 Hz to determine the linear viscoelastic region. Frequency sweeps were conducted at room temperature from 0.01 to 80 Hz with a strain amplitude of 0.25%. The mechanical properties obtained from these measurements should be considered as rough approximations to the mechanical properties of the lattice structure struts; the degree of polymerization for the lattice structures (polymerized by the 2PP instrument laser) is most likely different than that of these thin films (polymerized by a UV lamp).

Synchrotron-based Tomographic Imaging

Due to the time required to image a lattice in the laboratory, laboratory-based X-ray CT is limited to morphological deformation information before and after compression. This 'interrupted in situ' technique is described elsewhere [29-31]. In order to simultaneously collect the 3D morphological information during the compression, synchrotron X-ray CT is required. Several 2PP printed lattices were imaged using synchrotron X-ray CT at the Advanced Photon Source (APS) beamline 32-ID at Argonne National Laboratory. The high flux of the synchrotron allows researchers to collect full tomographic data sets in fractions of a second [29,26,16,32,33] and has been used to study a variety of in situ processes including loading, solidification, and electrochemical processes. The samples were imaged using a 20X objective after the 60 μm thick Lutetium Aluminum Garnet (LuAG) scintillator, which produced a field of view of 1 mm and a sample image pixel size of 1 μm on the camera. The stage was mounted on an air-bearing stage and was rotated at 7 Hz. 600 radiographs were collected during each 180º of rotation. Unfortunately, the load cell was not sensitive enough to measure the force for these small, soft materials; that data was not captured. Fourteen full 3D tomographic data sets were collected per second; approximately 20 CT's were collected during the in situ loading. The radiographic data was reconstructed into a folder of tiffs for each CT using TomoPy [34]. No binning of the data was necessary. Due to the low X-ray contrast, some manual segmentation was required. The choice of sample size and number of unit cells (2 x 2 x 2) for this study were primarily chosen due to the synchrotron imaging. The samples must be small enough so that image blur in 3D is minimized while maximizing strain rate. Larger samples would have required a larger displacement in the compression direction to obtain the same strain rate. This can be compensated for using iterative reconstruction techniques[35], and will be used in further experiments.

Image Processing

All 3D images (both laboratory and synchrotron-based CT) were processed using Avizo 9.2.0 (Thermo Fisher Scientific, Waltham, MA). The images were rendered, meshed, smoothed with the 'edge preserving smoothing' filter, and segmented. For the synchrotron data, the folders of the reconstructed tiffs from TomoPy were imported, filtered, and cropped using a custom, automated interface in Avizo. The microstructure for the FEM was obtained directly from the CT data, which was converted to STL files. The STL mesh was repaired to make it "watertight" using Meshlab (ISTI-CNR, Italy) [36]. This "watertight" mesh structure was discretized with tetrahedrons and imported into Abaqus.

Experimental Results

High resolution image was collected on the microCT of a lattice to measure the uniformity of the ligament diameter. The average diameter of the vertical struts is 32.2 μm. This is the average for multiple sets of ligaments, however with one set of nine vertical ligaments within one print, the standard deviation of the diameter is 0.13 μm, for different sets of nine ligaments, the standard deviation increases to 0.31 μm. The similitude between the ligaments is very high.

As seen in Figures 2 and 3, the laboratory-based X-ray CT images show the complete printing of the lattice structures as renderings in 3D before and after compression. The 2PP printer created complete structures that do not contain any interior voids (planned or unplanned). Additionally, the images of the compressed lattice structures show that the structures are fairly pliable. At 15% compression, deflections are seen in the ligaments and some damage has occurred; ligament breakage is sporatic. The compression of the various samples by the laboratory-based X-ray CT shows an interesting pattern in that the samples typically deform in a binary fashion. The load resulted in compression of either the top or the bottom layer of the sample, as seen in Figure 2. Not until the sample with 14.6% of the ligaments removed (Figure 3d) does the compression become distributed throughout the structure.

As shown in Figure 4 for the 10.1% missing ligament sample, the 5% strain compression cycles are reproducible, indicating that no cycle-to-cycle damage is occurring to the sample in this range of compression. However, during the first compression to 15% strain, the slope of the stress-strain curve becomes nonlinear at approximately 8% strain, and more obvious damage can be observed at approximately 11% strain. For the 50% strain cycle, roughness in the stress-strain curve indicates additional damage occurring within the structure. Figure 5 shows that similar damage occurs during the first compression to 15% strain for the samples with 0%, 5.1%, and 14.6% missing ligaments. Figure 5 also suggests that the Young's modulus decreases as the percentage of missing ligaments increases. To explore this dependence further, Figure 6 plots the average Young's modulus for samples with 0 - 25% missing ligaments. As stated in the Experimental section, these modulus values were averaged over the 5% strain cycles and the first 15% strain cycle, generally using data within the range of 3 - 9% strain. As the number of missing ligaments increases, the Young's modulus decreases in an almost linear fashion, though some nonlinearity is suggested near the 10.1% missing sample. To better understand this potential nonlinearity and determine which types of ligaments contribute most to the mechanical strength of these lattices, future experiments will examine structures with additional % missing values and structures created by only removing one type of ligament.

Figure 7 shows a series of sequential 3D CT images taken from the compression of the 25% missing sample using the APS synchrotron. It is the same structure as Figures 2e and 3e, but the image has been rotated to show the bending, buckling, and snapping of the ligament indicated by the red arrow. The series of images represent the (a-f) 0^{th} CT at 0% compression, 2^{nd} CT at 7% compression, 4^{th} CT at 14% compression, 6^{th} CT at 21% compression, 8^{th} CT at 28% compression, and 10^{th} CT at 35% compression loading. These 3D images are 140 milliseconds apart in time. The total time to collect the 3D images and compress to 35% was approximately 1.5 seconds, corresponding to a strain rate of ~0.4 s^{-1}. The reader is pointed to the red arrow showing the deformation of a ligament from a straight line into the shape of an ‘S’ and then the snapping of the ligament at the location of greatest stress just inside of the node connection. Future synchrotron experiments will focus on developing a more sensitive load cell in order to

capture the change in the stress that results from individual ligaments snapping (as suggested by the dips observed in the 50% strain cycle of Figure 4) while imaging in real-time.

Finite Element Analysis

Foam mechanical performance can be modeled with a variety of techniques. Many types of foams, including polymeric [37,38,4] and metallic foams [39,13], are modeled using the finite element method (FEM). X-ray CT provides a clear picture of the deformation of the material, and the bulk mechanical response is reported through the stress-strain measurement, but these data cannot convert the bulk strain to a local strain and then subsequently predict material failure. FEM can provide additional insight regarding the stress distribution throughout the material. Understanding the stress distribution allows engineers to better design the structure to minimize peak stress concentration and reduce onset of damage.

Material model

To model the polymeric material that comprised the ligaments in the lattice structures, the bulk shear modulus (G) was calculated from the DMA-measured tensile modulus (E) by (1):

$$G = E/(2 * (1 + v)) \qquad (1)$$

where v is the Poisson coefficient, and an isotropic, incompressible material is assumed. For incompressible materials, v is 0.5 and G ≅ E/3.

During the deformation of the lattice structure, strain is not evenly distributed through the ligaments, causing local increases in strain and predictable failure. A nonlinear-elastic material model, in this case a Neo-Hookean model [40] available in Abaqus, was used here. This was combined with viscoelastic behavior as described by a Prony series [41]:

$$G(t) = G_\infty + \sum_{i=1}^{M} G_i^{-t/\tau_i} \ , \qquad G_0 = G_\infty + \sum_{i=1}^{M} G_i \qquad (2)$$

where τ_i represents the relaxation times, G_∞ is the long term shear modulus and G_0 represents the instantaneous modulus. The coefficients G_i listed in Table 2 were extracted from the DMA data, as described above and shown in Figure 8.

Table 2

N	∞	1	2	3	4
G_i(MPa)	230.48	69.94	51.48	54.28	30.52
τ_i(s)		10.0	1.0	0.1	0.01

Neo-Hookean model: coefficients $C_{10} = G_0/2$, $G_0 = 436.69$ MPa and $D_1 = K_0/2$ where $K_0 = 3.7$ GPa.

Analysis

For the FEM analysis, the geometry of the foam was extracted from X-ray CT as a STL file, as shown in Figure 9a. Compression analysis in the z-direction was performed using Abaqus (Abaqus, Dassault Systèmes Simulia Corp, Providence, RI.). The structure was simply supported in the z-direction and subjected to a uniform strain rate of 0.0053 s^{-1} by applying displacement boundary conditions on the top surfaces as shown in Figure 9b. The analysis was conducted

using implicit time integration. Images of the deformed structures are shown in Figure 9c. Comparing this analysis with the experimental stress-strain data, the numerical stress-strain of the structure in the z-direction was determined by dividing the reaction force in z-direction by the cross-sectional area of the structure. As in the experiments, the strain represents the total deformation of the structure, considering a uniform strain rate.

The FEM analysis showed large deformation of the elements, similar to those observed experimentally (Figure 3). These deformations within the structure indicate a nonlinear response prior to collapse and densification. These aspects will be addressed in future work. For this manuscript, we only examined the initial linear response of the structure, focusing on the relationship between the numerical modeling and the initial experimental stress-strain data. Figure 10 shows the numerical stress-strain data for strain up to 0.1, and the results are similar to the experimental results shown in Figure 5. The small size of these samples presents unique experimental challenges, especially regarding sample loading and establishing full contact with the platens. Once full contact is established (strain ~ 0.03, Figure 5), the mechanical response of the structure becomes linear (through strain ~ 0.06 - 0.09, depending on the sample). In the FEM analysis, displacements were applied beginning at zero displacement (Figure 10) and the response of the structure under uniform strain rate was calculated. Numerical FEM analyses indicated that this linear response occurs immediately. Hence, the initial experimental compression (strain approx. < 0.03) does not compare well to the numerical simulation. However, the Young's modulus values calculated from the numerical data agree fairly well with the experimental values given in Figure 6. Beyond the linear range of the Young's modulus, one expects geometrical nonlinear response.

Conclusions

3D printing at high resolution has provided a direct path to better understand material deformation and failure. 3D printing allows for the systematic study of materials by creating multiple replicates of far higher similitude than would be possible using traditional manufacturing techniques. Specific structural elements within these identical structures were then varied to probe material properties of interest. By combining different X-ray imaging modalities (lab and synchrotron-based techniques) and applying several analysis techniques, a more complete understanding is presented. For the first time, we have demonstrated the 3D printing of complete structures and their analysis using 3D X-ray synchrotron tomography during in situ deformation. These CT techniques deliver a complete visual record of the complex interplay of material dynamics. Coupling this in situ visualization with stress-strain measurements delivers orthogonal material information and provides a more complete picture of the material properties at the individual ligament scale. Importing the CT images and modeling them directly provides a direct validation and understanding of a model's robustness because a side-by-side comparison on a ligament-by-ligament scale is now possible. Together, this framework allows scientists to further study how individual decisions on 3D structural design affect the bulk properties and to predict bulk material failure based on the ligament size scale. Future experiments will include further developing the in situ measures to acquire low force measurements simultaneously with the 3D imaging and to track the individual buckling of a ligament in both the 3D image and the stress-strain curve. The use of 2 x 2 x 2 unit cells was chosen to balance print time (one print per day) with the need for the sample to fit within the field of view of the synchrotron beam. This does reduce the applicability of the measurement to real-world predictions, however work is underway in printing larger structures. Future modeling

efforts will also address the buckling, post-buckling and densification problem through the analysis of the joint type (i.e. the points where the beams of the structure join). It expected that that region of material accumulation during printing around the joints will affect the critical buckling load.

Acknowledgements:

Funding for this research was provided by the Los Alamos Institute for Materials Science Rapid Response Program proposal RR1600BP; the LANL Engineering Campaign, the LANL Dynamic Materials Program (Josh Coe, Project Manager) and the LANL Joint Munitions Program (Matt Lewis, Project Manager). Los Alamos National Laboratory is operated by Triad National Security, LLC, for the National Nuclear Security Administration of U.S. Department of Energy (Contract No. 89233218NCA000001). This research used resources of the Advanced Photon Source, a U.S. Department of Energy (DOE) Office of Science User Facility operated for the DOE Office of Science by Argonne National Laboratory under Contract No. DE-AC02-06CH11357.

Figure Captions:

Figure 1: 3D rendering of the STL file with color-coding of the ligament classes. Details of the missing ligaments for the different structures are shown numerically in Table 1.

Figure 2: X-ray CT images of the five lattice structures that were printed: a) 0%, b) 5.1%, c) 10.1%, d) 14.6%, and e) 25.3%.

Figure 3: 3D tomographic images of the five samples that were printed and compressed to 15% strain: a) 0%, b) 5.1%, c) 10.1%, d) 14.6%, and e) 25.3%. At this loading, deflections are seen in the ligaments, but no breakage is obvious in the images. Interestingly, the compression for the 'more complete' lattices (a-c) is absorbed by either the top or the bottom layer. Some of the broken ligaments are shown by the red arrow.

.

Figure 4: Full stress-strain curves showing the complete loading profile used during compression with the nano-mechanical test stage for the 10.1% missing sample. Five cycles of compression to 5% strain were followed by five cycles to 15% strain, with a final compression to 50% strain.

Figure 5: The first 15% compression cycle for samples with 0%, 5.1%, 10.1%, and 14.6% missing ligaments. Nonlinearity in the stress-strain curves begin near 8 - 9% strain, and obvious damage can be observed in the range of 9 - 12% strain.

Figure 6: Young's modulus of the lattice structures with 0 - 25% missing ligaments, calculated from compression data obtained with the nano-mechanical test stage. Error bars represent the average over the five cycles to 5% strain and the first cycle to 15% strain.

Figure 7: Rendering of the 25.3% missing lattice structure imaged during in situ synchrotron imaging and compression. The figure represents every other image collected to approximately 35% compression. All of the 3D images presented here were collected within 1.5 seconds total. The red arrow highlights one particular ligament that is initially sloped at 45% in the upward direction, is nearly inverted in its slope, with a large strain at the node, that then finally snaps. The breakage is not seen in the previous image (which is between e and f), and occurs in less than 0.07 seconds.

Figure 8: (a) Storage and loss tensile moduli as function of frequency. (b) Shear modulus vs. time.

Figure 9: 3D rendering of the meshed lattice structures after importing into Abaqus: (a) CT-STL (b) represents the boundary conditions (colored regions reflect the loading), and (c) the rendered deformation at 13% compression.

Figure 10: Numerical simulations of the stress-strain measurements of the samples with 0%, 5.1%, 10.1%, and 14.6% missing ligaments. A) shows the numerical simulation results, B) compares the experimental and numerical simulation results for 0 and 14.6% missing, and C) shows the 5.1 and 10.1 % missing. The red arrows indicates the starting stress and strain, zeroed to remove the experimental data issues. See text for more details.

Compliance with Ethical Standards:
The authors declare that they have no conflict of interest.

References

1. Wallach JC, Gibson LJ (2001) Defect sensitivity of a 3D truss material. Scripta Materialia 45 (6):639-644. doi:http://dx.doi.org/10.1016/S1359-6462(01)01073-9

2. Patterson BM, Henderson K, Gilbertson RD, Tornga S, Cordes NL, Chavez ME, Smith Z (2014) Morphological and performance Measures of Polyurethane Foams using X-ray CT and Mechanical Testing. Microscopy and Microanalysis 95:18-26

3. Dattelbaum DM, Coe JD, Kiyanda CB, Gustavsen RL, Patterson BM (2014) Reactive, anomalous compression in shocked polyurethane foams. Journal of Applied Physics 115 (174908). doi:doi:http://dx.doi.org/10.1063/1.4875478

4. Ma Y, Su X, Pyrz R, Rauhe JC (2013) A novel theory of effective mechanical properties of closed-cell foam materials. Acta Mechanica Solida Sinica 26 (6):559-569. doi:http://dx.doi.org/10.1016/S0894-9166(14)60001-X

5. Gaitanaros S, Kyriakides S, Kraynik AM (2012) On the crushing response of random open-cell foams. International Journal of Solids and Structures 49 (19–20):2733-2743. doi:http://dx.doi.org/10.1016/j.ijsolstr.2012.03.003

6. Gibson LJ, Ashby MF (1997) Cellular Solids: Structure and Properties. Cambridge University Press, Cambridge

7. Ngo TD, Kashani A, Imbalzano G, Nguyen KTQ, Hui D (2018) Additive manufacturing (3D printing): A review of materials, methods, applications and challenges. Composites Part B: Engineering 143:172-196. doi:https://doi.org/10.1016/j.compositesb.2018.02.012

8. Vaezi M, Seitz H, Yang S (2013) A review on 3D micro-additive manufacturing technologies. The International Journal of Advanced Manufacturing Technology 67 (5):1721-1754. doi:10.1007/s00170-012-4605-2

9. Tumbleston JR, Shirvanyants D, Ermoshkin N, Janusziewicz R, Johnson AR, Kelly D, Chen K, Pinschmidt R, Rolland JP, Ermoshkin A, Samulski ET, DeSimone JM (2015) Continuous liquid interface production of 3D objects. Science. doi:10.1126/science.aaa2397

10. Walker DA, Hedrick JL, Mirkin CA (2019) Rapid, large-volume, thermally controlled 3D printing using a mobile liquid interface. Science 366 (6463):360-364. doi:10.1126/science.aax1562

11. Zheng X, Lee H, Weisgraber TH, Shusteff M, Deotte JR, Duoss E, Kuntz JD, Biener MM, Kucheyev SO, Ge Q (2014) Ultra-light, Ultra-stiff Mechanical Metamaterials. Science

12. Montemayor LC, Meza LR, Greer JR (2014) Design and Fabrication of Hollow Rigid Nanolattices via Two-Photon Lithography. Advanced Engineering Materials 16 (2):184-189. doi:10.1002/adem.201300254

13. Carlton HD, Lind J, Messner MC, Volkoff-Shoemaker NA, Barnard HS, Barton NR, Kumar M (2017) Mapping local deformation behavior in single cell metal lattice structures. Acta Materialia 129:239-250. doi:https://doi.org/10.1016/j.actamat.2017.02.023

14. Ladd AJC, Kinney JH (1997) Elastic constants of cellular structures. Physica A: Statistical Mechanics and its Applications 240 (1):349-360. doi:https://doi.org/10.1016/S0378-4371(97)00158-1

15. Ladd AJC, Kinney JH, Haupt DL, Goldstein SA (1998) Finite-element modeling of trabecular bone: Comparison with mechanical testing and determination of tissue modulus. Journal of Orthopaedic Research 16 (5):622-628. doi:10.1002/jor.1100160516

16. Patterson BM, Cordes NL, Henderson K, Williams J, Stannard T, Singh SS, Ovejero AR, Xiao X, Robinson M, Chawla N (2016) In situ X-ray synchrotron tomographic imaging during the compression of hyper-elastic polymeric materials. Journal of Material Science 51 (1):171-187. doi:DOI 10.1007/s10853-015-9355-8

17. Sercombe TB, Xu X, Challis VJ, Green R, Yue S, Zhang Z, Lee PD (2015) Failure modes in high strength and stiffness to weight scaffolds produced by Selective Laser Melting. Materials & Design 67:501-508. doi:http://dx.doi.org/10.1016/j.matdes.2014.10.063

18. Walley SM, Field JE (1994) Strain Rate Sensitivity of Polymers in Compression from Low to High Rates. Dymat Journal 1 (3):211-227

19. Shan G-F, Yang W, Yang M-b, Xie B-h, Feng J-m, Fu Q (2007) Effect of temperature and strain rate on the tensile deformation of polyamide 6. Polymer 48 (10):2958-2968. doi:http://dx.doi.org/10.1016/j.polymer.2007.03.013

20. Tucker MT, Horstemeyer MF, Whittington WR, Solanki KN, Gullett PM (2010) The effect of varying strain rates and stress states on the plasticity, damage, and fracture of aluminum alloys. Mechanics of Materials 42 (10):895-907. doi:http://dx.doi.org/10.1016/j.mechmat.2010.07.003

21. Chen Y, Clausen AH, Hopperstad OS, Langseth M (2009) Stress–strain behaviour of aluminium alloys at a wide range of strain rates. International Journal of Solids and Structures 46 (21):3825-3835. doi:http://dx.doi.org/10.1016/j.ijsolstr.2009.07.013

22. Sun PL, Cerreta EK, Gray GT, III, Bingert JF (2006) The effect of grain size, strain rate, and temperature on the mechanical behavior of commercial purity aluminum. Metallurgical and Materials Transactions A 37 (10):2983-2994. doi:10.1007/s11661-006-0180-1

23. Song B, Lu W-Y, Syn C, Chen W (2009) The effects of strain rate, density, and temperature on the mechanical properties of polymethylene diisocyanate (PMDI)-based rigid polyurethane foams during compression. Journal of Materials Science 44 (2):351-357. doi:10.1007/s10853-008-3105-0

24. Zaldivar RJ, Witkin DB, McLouth T, Patel DN, Schmitt K, Nokes JP (2017) Influence of processing and orientation print effects on the mechanical and thermal behavior of 3D-Printed ULTEM® 9085 Material. Additive Manufacturing 13:71-80. doi:https://doi.org/10.1016/j.addma.2016.11.007

25. Liljenhjerte J, Upadhyaya P, Kumar S (2016) Hyperelastic strain measurements and constitutive parameters identification of 3D printed soft polymers by image processing. Additive Manufacturing 11:40-48. doi:https://doi.org/10.1016/j.addma.2016.03.005

26. Mertens JCE, Henderson K, Cordes NL, Pacheco R, Xiao X, Williams JJ, Chawla N, Patterson BM (2017) Analysis of thermal history effects on mechanical anisotropy of 3D-printed polymer matrix composites via in situ X-ray tomography. Journal of Materials Science 52 (20):12185-12206. doi:10.1007/s10853-017-1339-4

27. Wang B, Sun L, Pan B (2019) Mapping internal deformation fields in 3D printed porous structure with digital volume correlation. Polymer Testing 78:105945. doi:https://doi.org/10.1016/j.polymertesting.2019.105945

28. Gardan J, Makke A, Recho N (2018) Improving the fracture toughness of 3D printed thermoplastic polymers by fused deposition modeling. Int J Fract 210 (1):1-15. doi:10.1007/s10704-017-0257-4

29. Patterson BM, Cordes NL, Henderson K, Xiao X, Chawla N (2018) Data Challenges of In Situ X-ray Tomography for Materials Discovery and Characterization. In: Lookman T, Eidenbenz S, Alexander F, Barnes C (eds) Materials Discovery and Design By Means of Data Science and Optimal Learning, vol 280. Springer, pp 130-158

30. Walters DJ, Luscher DJ, Yeager JD, Patterson BM (2018) Cohesive finite element modeling of the delamination of HTPB binder and HMX crystals under tensile loading. International Journal of Mechanical Sciences 140:151-162. doi:https://doi.org/10.1016/j.ijmecsci.2018.02.048

31. Manner VW, Yeager JD, Patterson BM, Walters DJ, Stull JA, Cordes NL, Luscher DJ, Henderson KC, Schmalzer AM, Tappan BC (2017) In Situ Imaging during Compression of Plastic Bonded Explosives for Damage Modeling. MDPI 10 (638). doi:doi:10.3390/ma10060638

32. Maire E, Le Bourlot C, Adrien J, Mortensen A, Mokso R (2016) 20 Hz X-ray tomography during an in situ tensile test. Int J Fract 200 (1):3-12. doi:10.1007/s10704-016-0077-y

33. Maire E, Withers PJ (2014) Quantitative X-ray tomography. International Materials Reviews 59 (1):1-43. doi:10.1179/1743280413Y.0000000023

34. Gursoy D, De Carlo F, Xiao X, Jacobsen C (2014) TomoPy: a framework for the analysis of synchrotron tomographic data. Journal of Synchrotron Radiation 21 (5):1188-1193. doi:doi:10.1107/S1600577514013939

35. Arcadu F, Marone F, Stampanoni M (2017) Fast iterative reconstruction of data in full interior tomography. Journal of Synchrotron Radiation 24 (1):205-219. doi:doi:10.1107/S1600577516015794

36. Cognoni P, Callieri M, Corsini M, Dellepiane M, Ganovelli F, Ranzuglia G MeshLab: an Open-Source Mesh Processing Tool. In: Sixth Eurographics Italian Chapter Conference, Pisa, Italy, 2008. pp 129-136

37. Youssef S, Maire E, Gaertner R (2005) Finite element modelling of the actual structure of cellular materials determined by X-ray tomography. Acta Materialia 53 (3):719-730. doi:https://doi.org/10.1016/j.actamat.2004.10.024

38. Lewis M (2016) A robust, compressible, hyperelastic constitutive model for the mechanical response of foamed rubber. Technische Mechanik 36 (1-2):88-101

39. Burteau A, N'Guyen F, Bartout JD, Forest S, Bienvenu Y, Saberi S, Naumann D (2012) Impact of material processing and deformation on cell morphology and mechanical behavior of polyurethane and nickel foams. International Journal of Solids and Structures 49 (19–20):2714-2732. doi:http://dx.doi.org/10.1016/j.ijsolstr.2012.05.026

40. Kim B, Lee SB, Lee J, Cho S, Park H, Yeom S, Park SH (2012) A comparison among Neo-Hookean model, Mooney-Rivlin model, and Ogden model for chloroprene rubber. International Journal of Precision Engineering and Manufacturing 13 (5):759-764. doi:10.1007/s12541-012-0099-y

41. Christensen R (2012) Theory of viscoelasticity: an introduction. Elsevier,

Figure 1

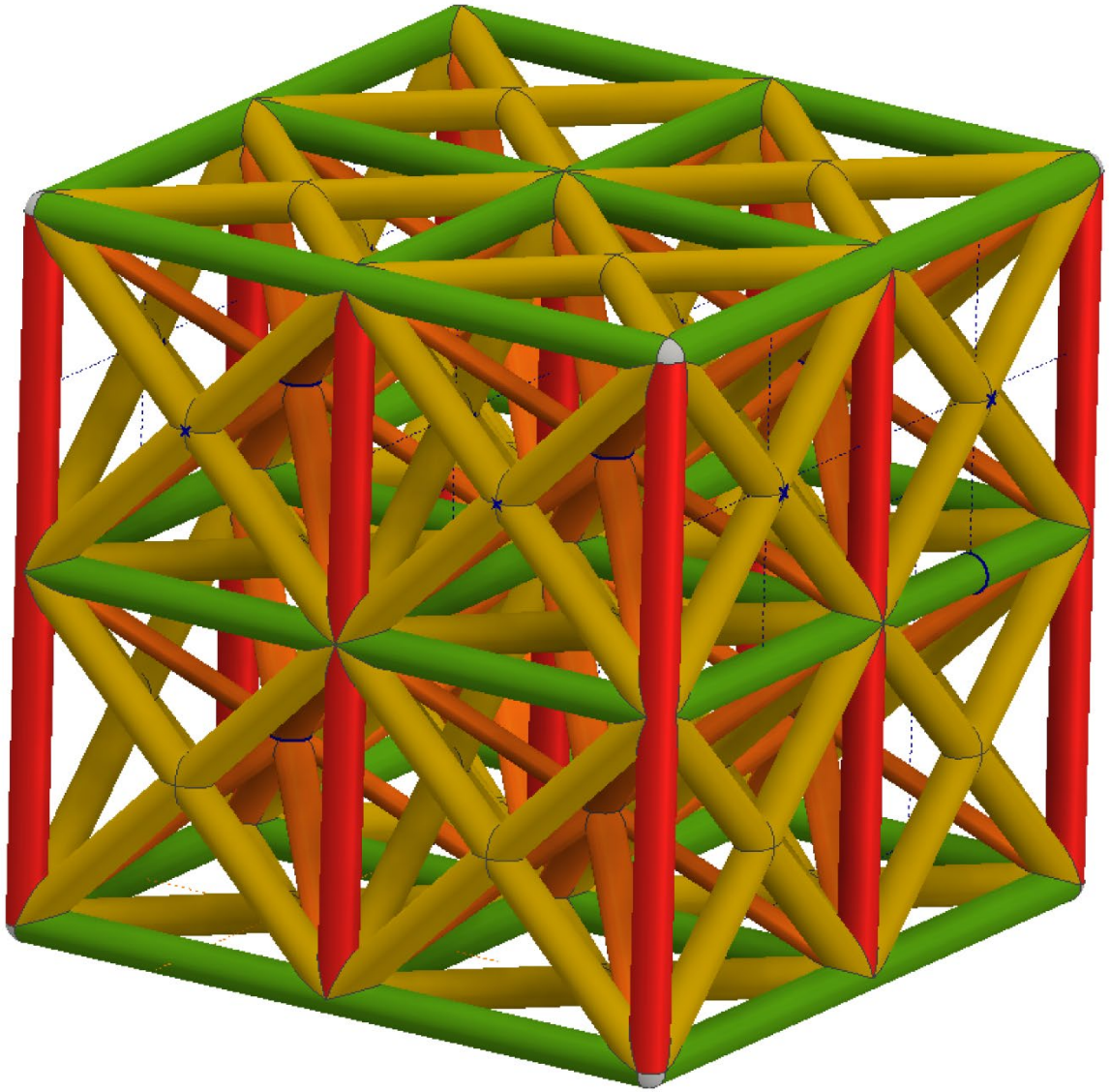

Figure 2

a)

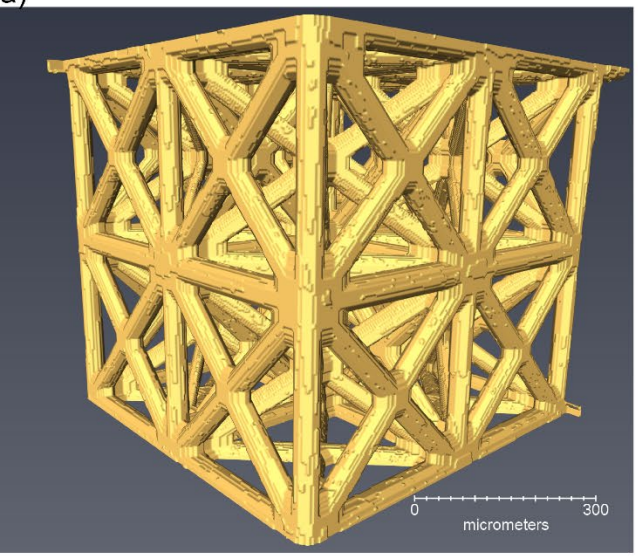

b)

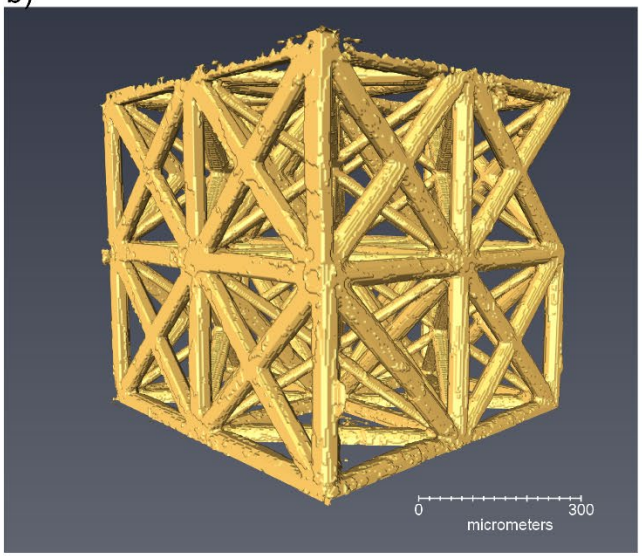

c)

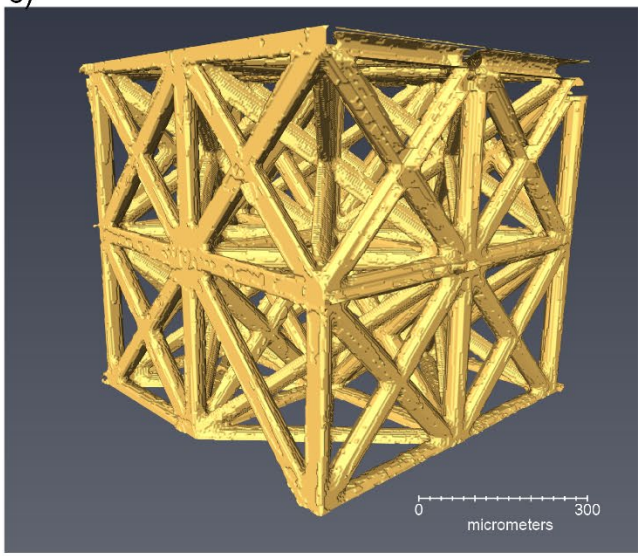

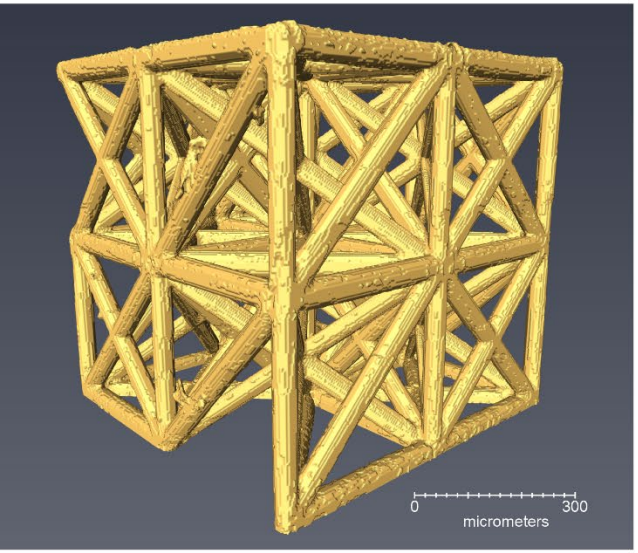

d)

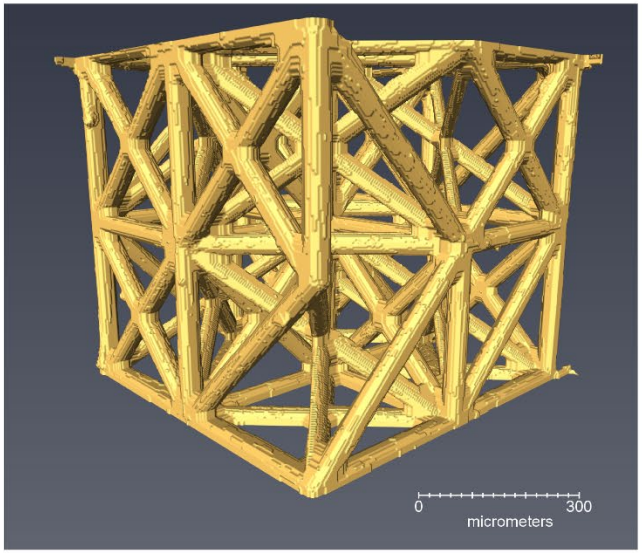

e)

Figure 3

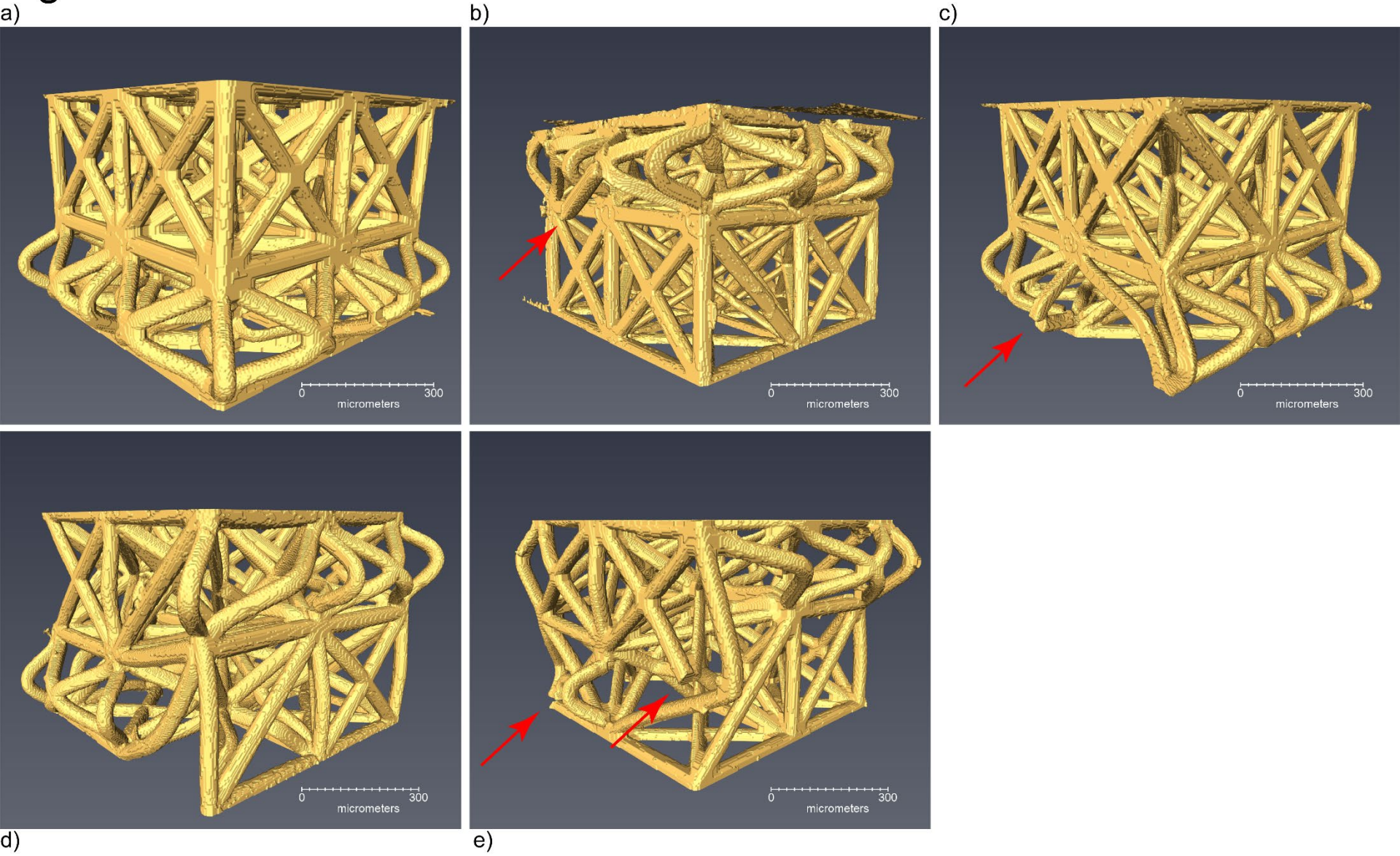

Figure 4

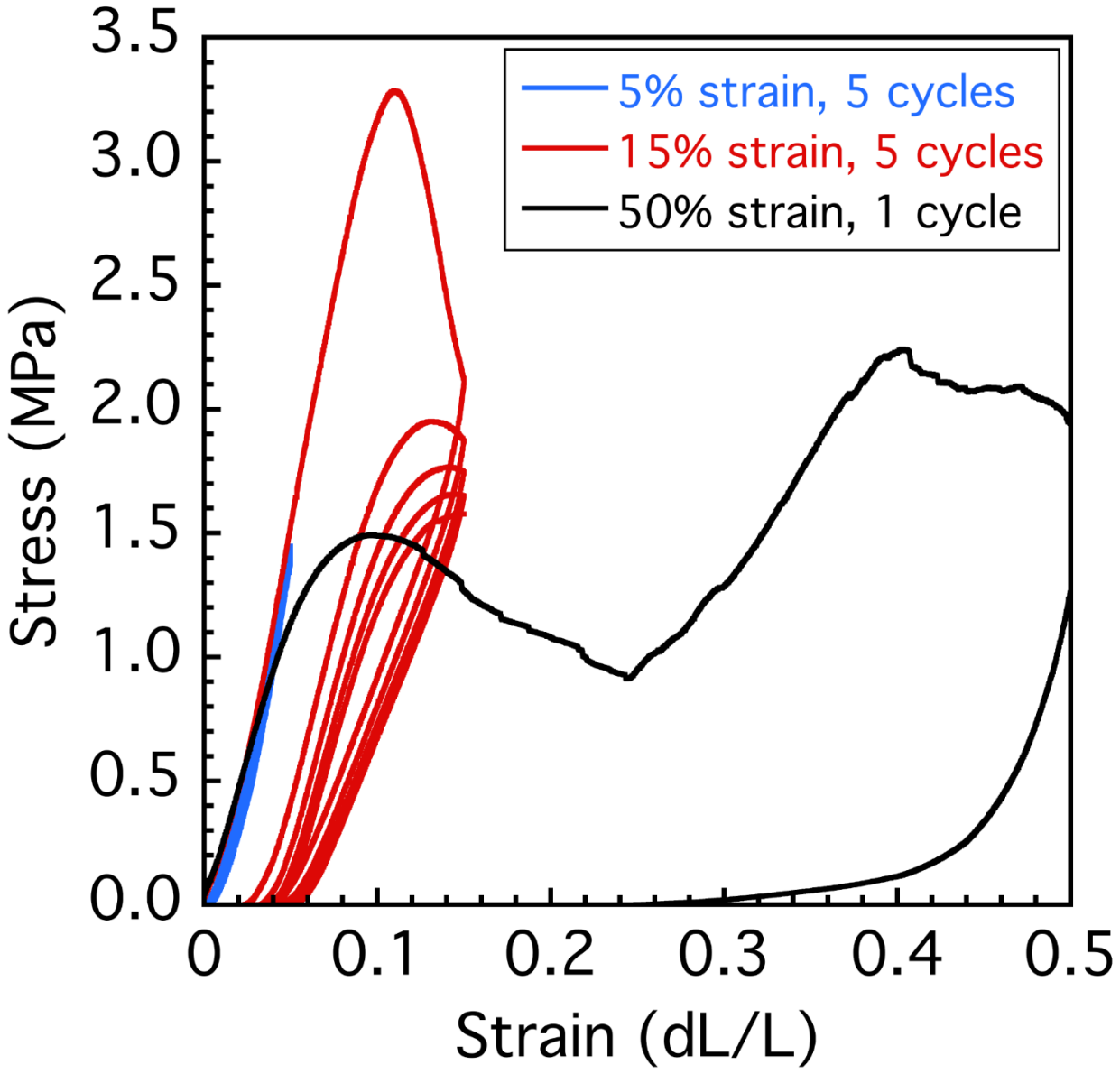
5% strain, 5 cycles
15% strain, 5 cycles
50% strain, 1 cycle
Stress (MPa)
Strain (dL/L)
0.0
0.5
1.0
1.5
2.0
2.5
3.0
3.5
0
0.1
0.2
0.3
0.4
0.5

Figure 5

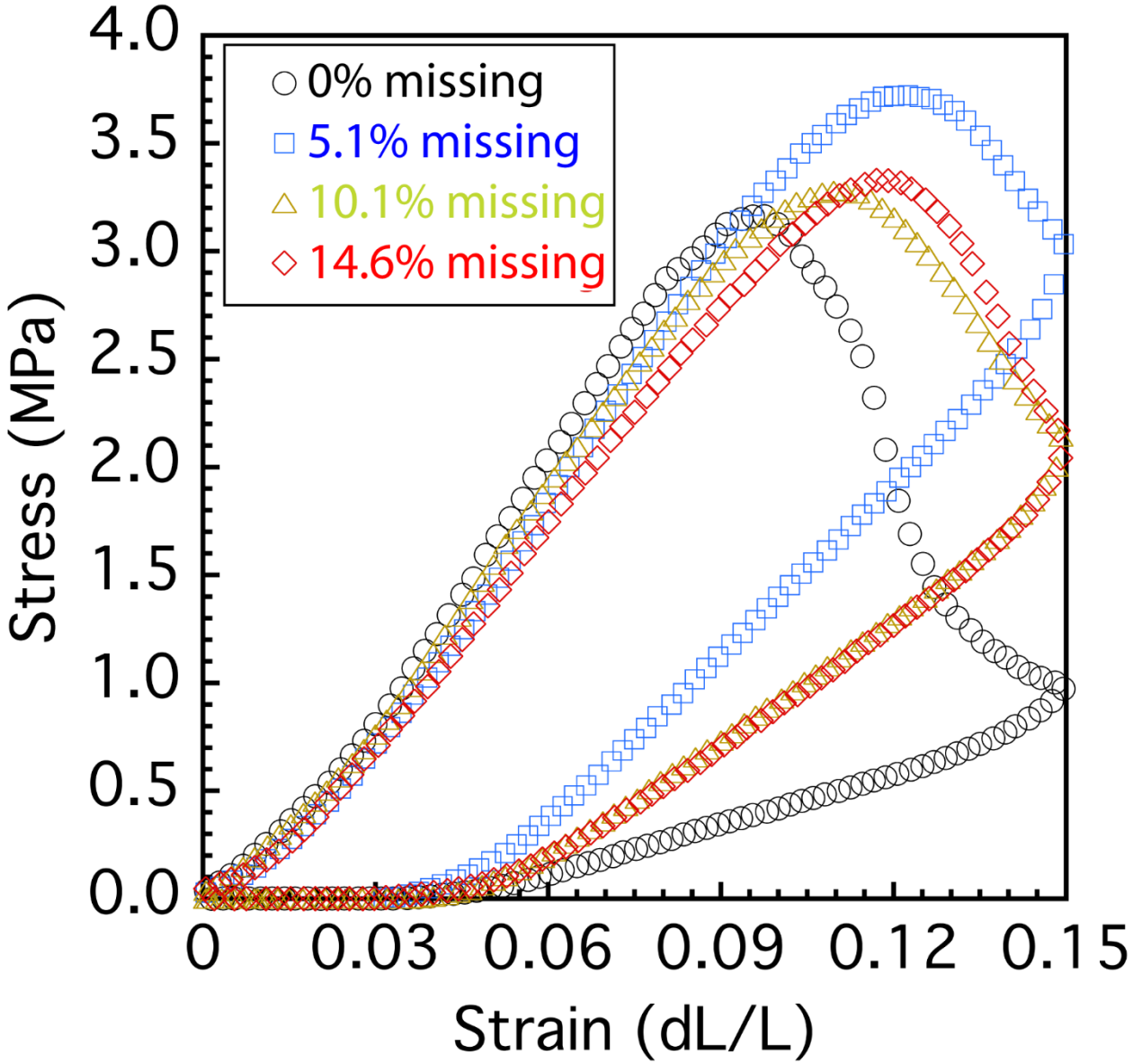
0% missing
5.1% missing
10.1% missing
14.6% missing
Stress (MPa)
Strain (dL/L)
0.0
0.5
1.0
1.5
2.0
2.5
3.0
3.5
4.0
0
0.03
0.06
0.09
0.12
0.15

Figure 6

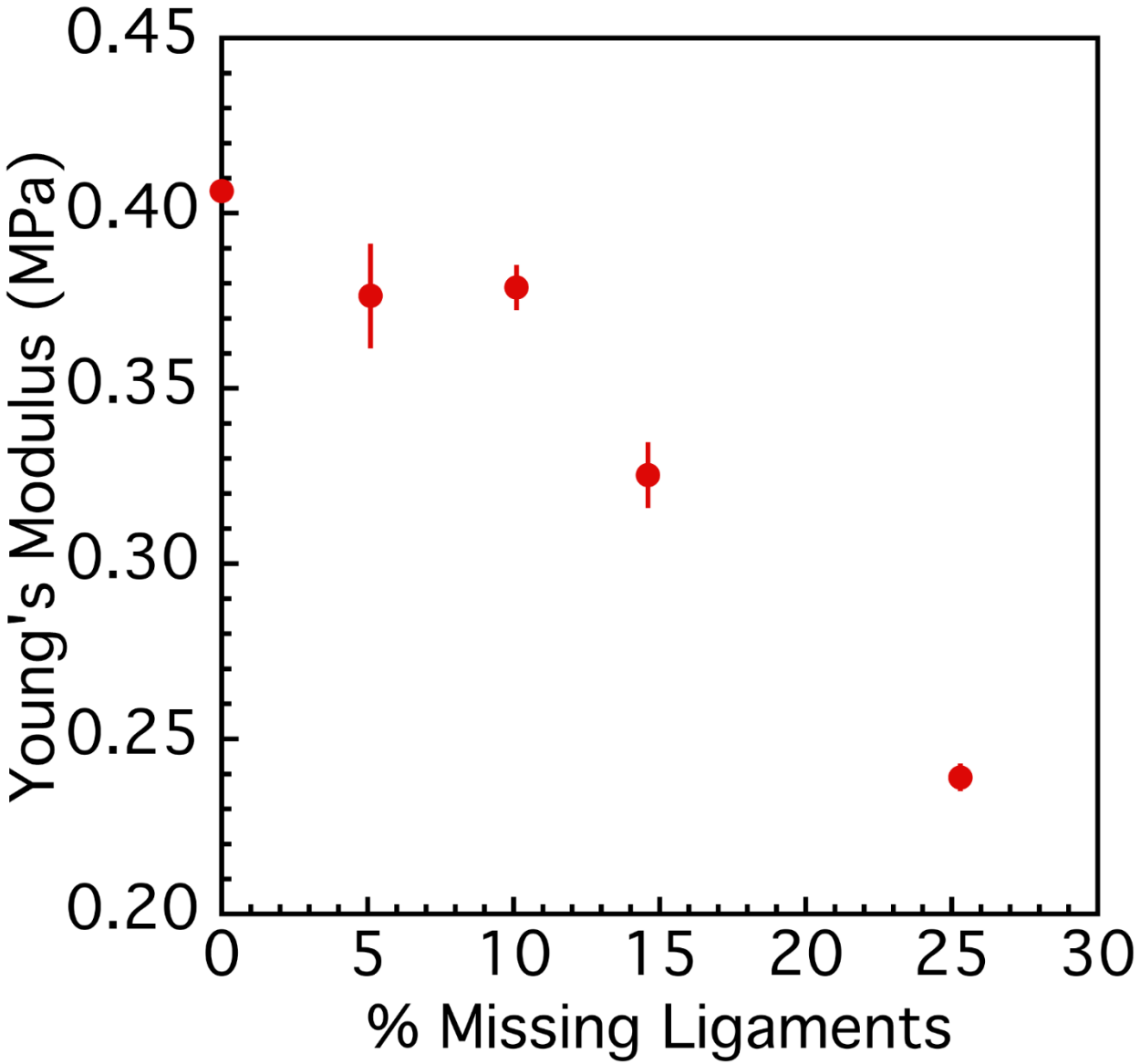
0.45
0.40
0.35
0.30
0.25
0.20
Young's Modulus (MPa)
0
5
10
15
20
25
30
% Missing Ligaments

Figure 7

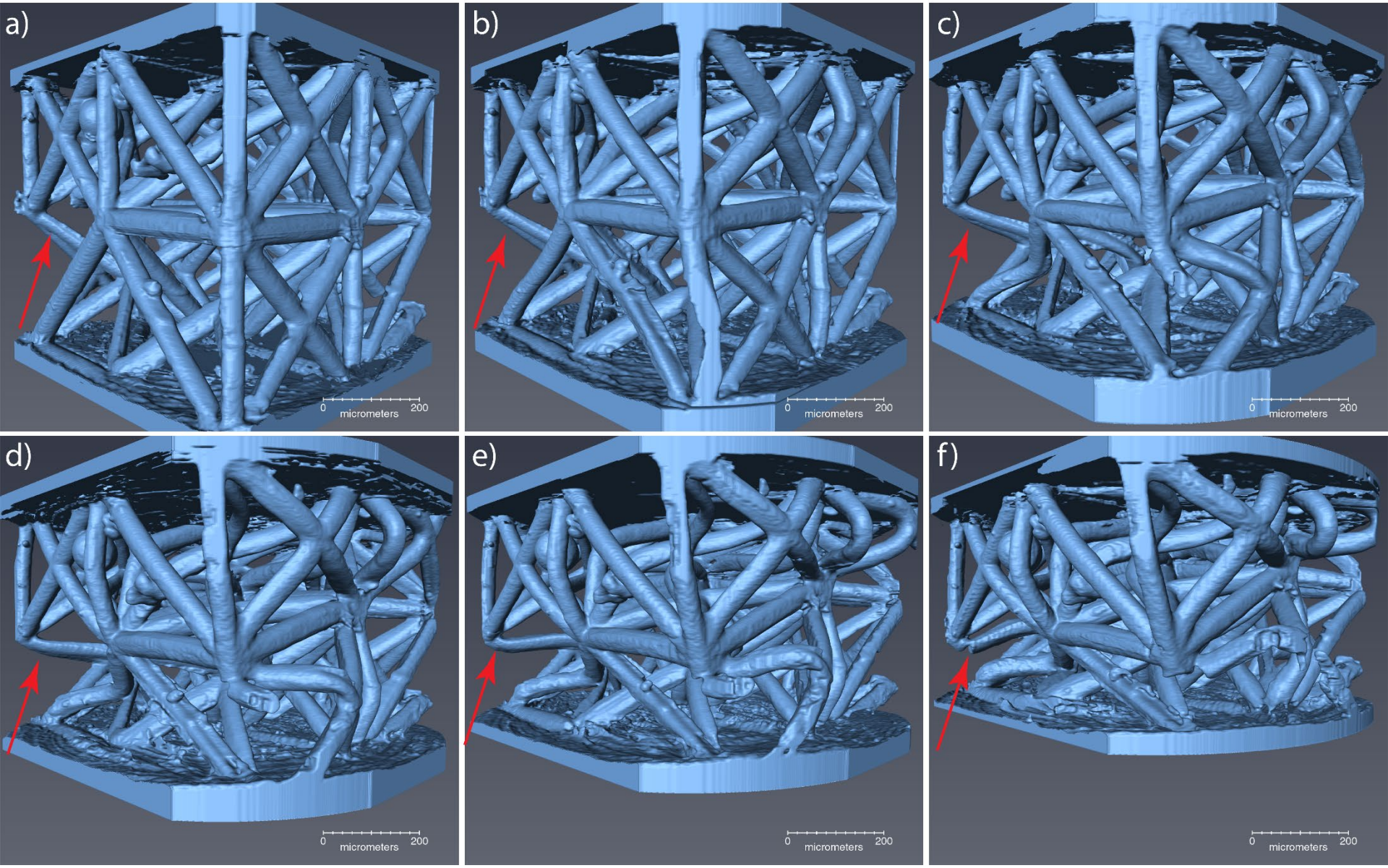
a)
0
micrometers
200
b)
0
micrometers
200
c)
0
micrometers
200
d)
0
micrometers
200
e)
0
micrometers
200
f)
0
micrometers
200

Figure 8

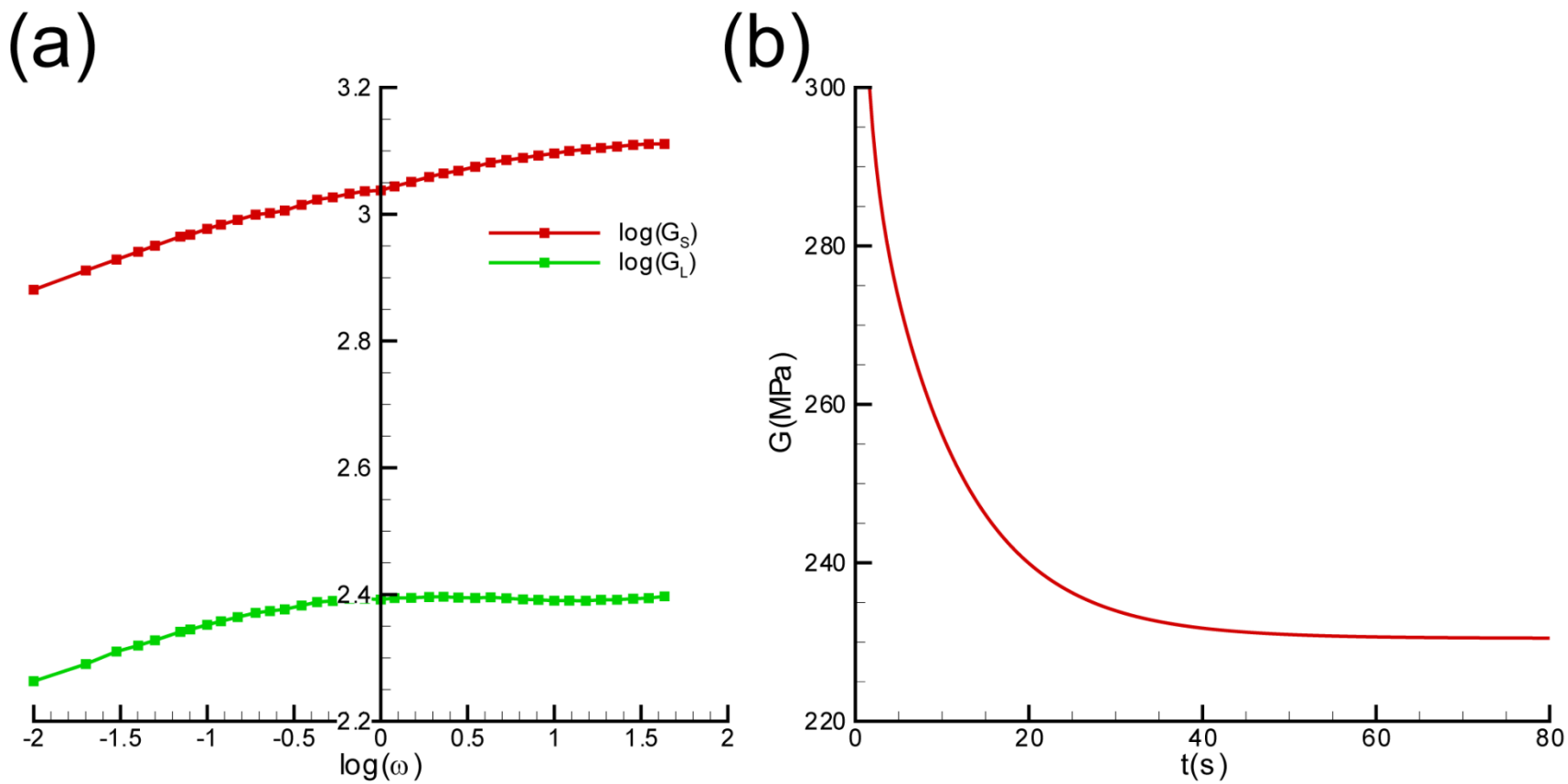
(a)
3.2
3
2.8
2.6
2.4
2.2
log(G_S)
log(G_L)
-2
-1.5
-1
-0.5
0
0.5
1
1.5
2
log(ω)
(b)
300
280
260
240
220
G(MPa)
0
20
40
60
80
t(s)

Figure 9

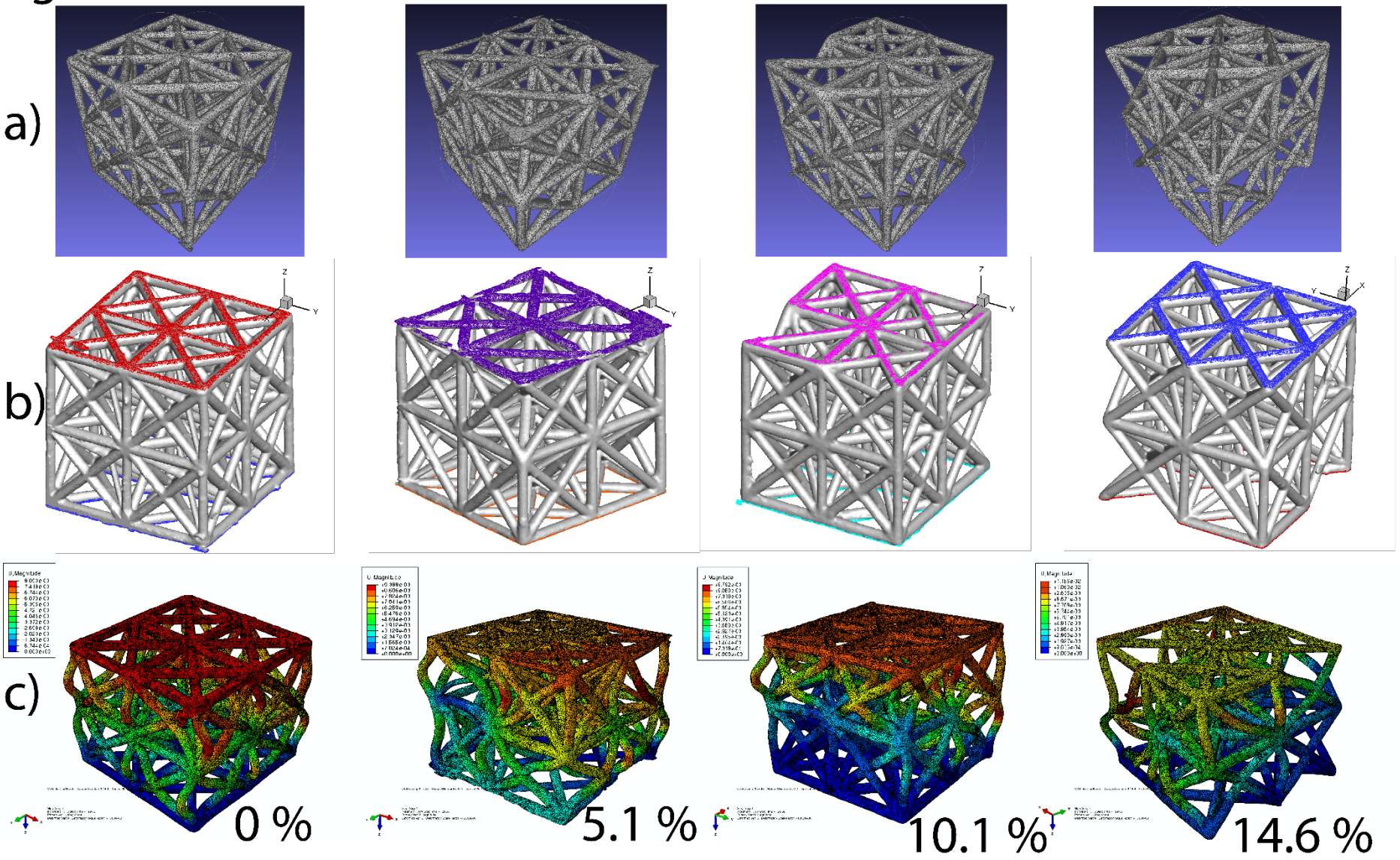

Figure 10

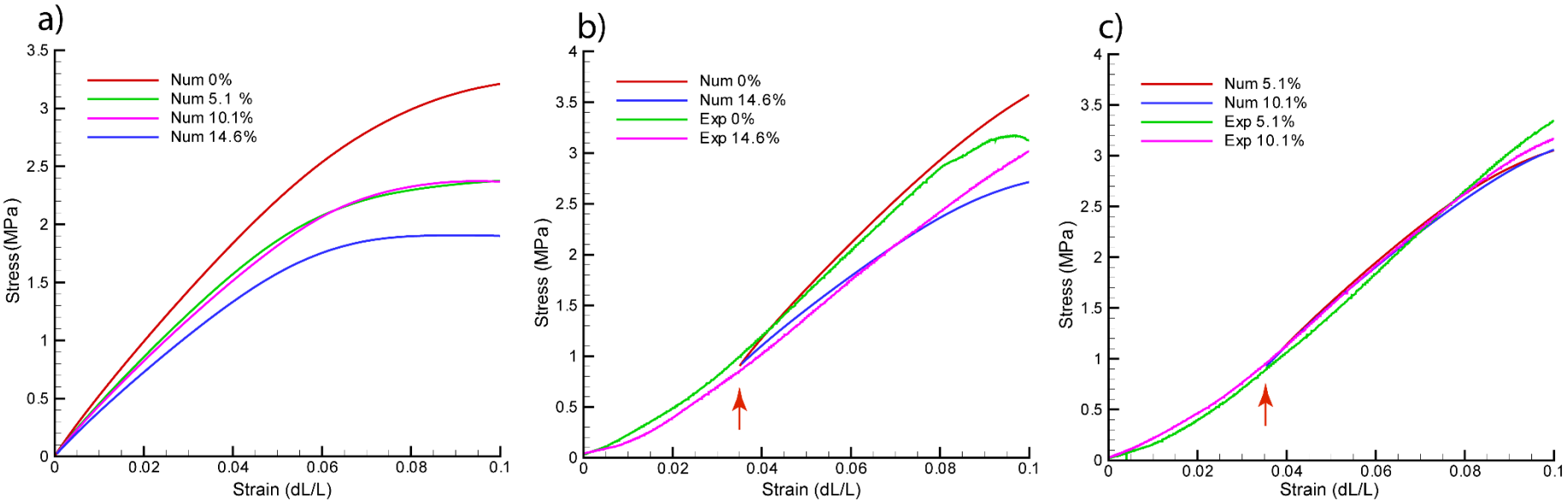
a)
Num 0%
Num 5.1 %
Num 10.1%
Num 14.6%
Stress (MPa)
Strain (dL/L)
b)
Num 0%
Num 14.6%
Exp 0%
Exp 14.6%
Stress (MPa)
Strain (dL/L)
c)
Num 5.1%
Num 10.1%
Exp 5.1%
Exp 10.1%
Stress (MPa)
Strain (dL/L)